Structural, Morphological and Magnetic Investigation of Half-Doped La0.5Ba0.5MnO3 Perovskite Nanoparticles

[1]Yusuf Samancıoğlu (iD)

[1]Muğla Sıtkı Koçman University, Vocational School of Health Services, Department of Medical Services and Techniques, Opticianry, Marmaris, Muğla, Turkey.

Corresponding author, e-mail: ysamancioglu@mu.edu.tr , https://orcid.org/0000-0002-3540-5011

Abstract: This study investigated the effect of barium (Ba) substitution for lanthanum (La) on the magnetic properties of the half-doped perovskite manganite compound $La_{0.5}Ba_{0.5}MnO_3$ (LBMO). The LBMO sample was prepared via the sol-gel method and sintered in air at 1000°C for 24 hours. Scanning electron microscopy (SEM)-energy dispersive X-ray spectroscopy (EDS) analysis revealed random formation of $BaMnO_3$ nanorods on the LBMO surface. The LBMO perovskite exhibited a particle size distribution of approximately 60 nm, while the $BaMnO_3$ nanorods possessed widths ranging from 100-250 nm and lengths between 5-20 µm. X-ray diffraction (XRD) analysis found that the main perovskite compound (LBMO) exhibits a cubic crystal structure (a = 3.9108 Å), while the nanorods ($BaMnO_3$) possess a hexagonal crystal structure (a = 5.6454 Å, c = 4.8224 Å). The Curie temperature (T_C) was determined to be approximately 323 K, close to room temperature, zero field cooling (ZFC) and field cooling (FC) curves to elucidate the magnetic properties. Furthermore, magnetization measurements yielded a magnetic entropy change ($\square\Delta S_M$) of 0.62 J/kgK at 1 T and 2.25 J/kgK at 6 T.

Keywords: Half-doped perovskite manganites, $BaMnO_3$, nanorods, Curie temperature

Yarı-Katkılı La0.5Ba0.5MnO3 Perovskit Nanoparçacıklarının Yapısal, Morfolojik ve Manyetik Özelliklerinin İncelenmesi

Öz: Bu çalışma $La_{0.5}Ba_{0.5}MnO_3$ (LBMO) yarı katkılı perovskit manganit bileşiğinde lantan (La) yerine baryum (Ba) yer değişiminin manyetik özellikleri üzerindeki etkisi araştırıldı. Numune sol-jel yöntemi kullanılarak hazırlandı ve 1000°C'de 24 saat ısıl işleme tabi tutuldu. Taramalı elektron mikroskobu (SEM)-enerji dağılım spektroskopi (EDS) analizi LBMO yüzeyinde rastgele $BaMnO_3$ nano çubuk oluşumunu ortaya çıkardı. LBMO perovskit bileşiğinin parçacık boyutu dağılımının yaklaşık 60 nm olduğu bulundu. Ayrıca, analizler sonucunda $BaMnO_3$ nano çubukların genişliği 100-250 nm ve uzunluğu 5-20 µm aralığında değiştiği gözlendi. X-ışını kırınımı (XRD) analizi, ana perovskit bileşiğinin (LBMO) kübik kristal yapıda (a= 3.9108 Å) olup, nano çubukların ise altıgen (a=5.6454 Å, c=4.8224 Å) kristal yapıya sahip olduğu gösterildi. Manyetik özelliklerin ortaya konabilmesi için sıfır alan soğutma (ZFC) ve alan altında soğutma (FC) eğrilerinden yararlanarak Curie sıcaklığını oda sıcaklığına yakın (T_C) 323 K olduğu tespit edildi. Mıknatıslanma ölçümleri verileri kullanılarak hesaplanan manyetik entropi değişiminin ($-\Delta S_M$), 1 T'de 0,62 J/kgK ve 6 T'de 2,25 J/kgK olduğu bulundu.

Anahtar kelimeler: Yarı katkılı perovskit manganitler, BaMnO3, nanoçubuklar, Curie sıcaklığı.

Graphical Abstract:

---
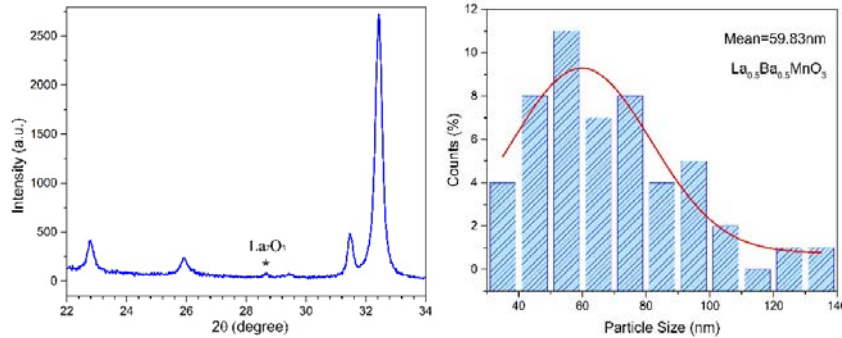
[1] Corresponding author: Tel: 0 252 211 56 22
E-mail: ysamancioglu@mu.edu.tr

1. Introduction

Perovskite oxides are a class of materials with the general formula ABO_3, where A^{3+} and B^{2+} are metal cations and O^{2-} is oxygen. These materials have attracted significant attention in recent years due to their diverse and intriguing electronic, magnetic, and structural properties. One of the most promising members of this family is $La_{1-x}A_xMnO_3$ ($A=Ca^{2+}$, Sr^{2+}, Ba^{2+},...etc.), a half-doped perovskite manganite $La_{0.5}Ba_{0.5}MnO_3$ (LBMO) with a Curie temperature close to room temperature [1]–[3]. Previous studies have selected half-doped perovskites of this type for the creation of dielectric ferromagnets with high-frequency properties and self-magnetization. Additionally, they are being investigated due to their high magnetoresistance and manyetocaloric properties. The nature of perovskite manganites is not fully understood [4]. This makes LBMO a promising candidate for a wide range of applications, including spintronic devices, magnetic sensors, catalytic materials, and other electronic devices [5-8]. Differences in the cations of the perovskite compound as a result of Ba substitution for La have also been reported in literature studies. One of the key factors that influences the properties of $La_{0.5}^{3+}Ba_{0.5}^{2+}Mn_{0.5}^{3+}Mn_{0.5}^{4+}O_3^{2-}$ is the ratio of La^{3+} to Ba^{2+} cations. For this compound, the ionic radius incompatibility and the presence of complex valences cause the manganite structure to exhibit a complex phase diagram and contain multiple phases together [9]. Ba^{2+} substitution for La^{3+} leads to a number of changes in the manganese atoms (Mn^{3+}, Mn^{4+}), including increased carrier concentration, reduced lattice distortion, and enhanced ferromagnetism. And then T_C of these perovskite compounds exhibits a strong dependence on the Mn^{3+}/Mn^{4+} ratio [10]. In addition, the atomic radius of the Ba^{2+} atom is quite larger than La^{3+}, so Ba^{2+} substitution can also cause the formation of $Ba^{2+}Mn^{4+}O_3^{2-}$ through a process known as self-assemble. Literature reports suggest that upon approaching designated doping rates, the manganese ions in the 50% Ba-substituted perovskite compound exhibit changes in their valence state. This phenomenon is further reinforced by the application of high-temperature heat treatment under atmospheric conditions, leading to valence fluctuations in manganese ions (Mn^{2+}, Mn^{3+}, Mn^{4+},…etc.) exceeding a 47% doping contribution rate[9]–[12]. In the case of LBMO, the second phase is $BaMnO_3$ (BMO), which forms during the sol-gel synthesis process [13]. The sol-gel method is widely used for producing bulk perovskite manganite compounds due to its cost-effectiveness, ease of synthesis, and ability to produce homogeneous samples, as well as for allowing adjustments in transition temperatures through various element doping rates. The hydrothermal synthesis method is frequently used in the literature for the production of LBMO and BMO perovskite nanorods or nanocrystals [14]. However, it is reported that this synthesis method suffers from limitations, particularly in controlling particle size and shape, as well as achieving a homogeneous distribution due to the emergence of undesirable impurities during production [15]–[18]. In this study, the structural, morphological and magnetic properties of the LBMO compound produced by the sol-gel method were comprehensively examined. The formation of nanorods on LBMO can have a significant impact on the magnetic properties of the material. It is known that materials reduced to nano size have different chemical and physical properties than their bulk counterparts [17]. Today, it is reported in the literature that perovskite manganites, which are very difficult to produce at nanoscale, exhibit different magnetic and electrical properties and that obtaining magnetic nanosensors has become difficult due to the inability to provide a stable electronic balance in these compounds [19]. $BaMnO_3$ nanorods on the compound surface exhibit antiferromagnetic properties by creating new magnetic interactions [20]. In addition, the nanorods can also be used to tailor the magnetic properties of LBMO for specific applications. Although it has been understood late that the antiferromagnetic properties occurring in perovskite manganite materials can be used, compounds such as perovskite ($BaMnO_3$–$LaMnO_3$–$LaFeO_3$) can be used in spintronic devices, solid oxide fuel cells (SOFC), energy storage, electrodes, dielectric materials and drug delivery [13], [17], [21]. We believe that our study will provide new insights into the relationship between Ba substitution and the formation of $BaMnO_3$ nanorods in LBMO. Our

23

findings will also be valuable for the development of LBMO-based materials with tailored magnetic properties for particular applications.

2. Materials and Methods

The LBMO sample was synthesized using the sol-gel method and utilization of consumables of high purity was employed, including 99.9% La_2O_3 (Sigma-Aldrich), 98.5% $Mn(NO_3)2x4H_2O$ (Merck), 99% $Ba(NO_3)_2$ (Merck). To initiate the synthesis, the consumables were dissolved in a solution containing HCl and NHO₃. The resulting solution was mixed using a magnetic heater stirrer at a temperature of 150°C. Subsequently, ethylene glycol and citric acid were added to the mixture, and the temperature was raised to 300°C, resulting in gelation. After the gelation process was completed, the organic compounds were eliminated by subjecting the gel to burn at 600°C for 12 hours. The resulting powder compound was then ground in an agar mortar for 6 hours to ensure homogeneity and optimized distribution. To prepare the sample for analysis, approximately 1 gram of the powder was accurately weighed and pressed into a mold with a diameter of 13 mm and a thickness of 2 mm, applying a pressure of 3 bar. The bulk sample was subsequently heat treatment (controlled with a temperature increase of 5.5 °C per minute) in a 1000 °C furnace for 24 hours to enhance its crystallinity and stability. The crystal structure of the synthesized samples was formed during heat treatment [28]. To investigate the crystallographic characteristics of the samples, X-ray diffraction (XRD) measurements were conducted using the Rigaku SmartLab X-ray diffractometer. The samples were placed in the diffractometer and scanned at room temperature, covering an angular range between 20 to 100 degrees with a precise step size of 0.01 degrees. Surface analysis of samples subjected to 24 hours heat treatment at 1000°C which was using Jeol 7600F Scanning Electron Microscope (SEM). This advanced SEM allows for high-resolution imaging of sample surfaces at different magnifications and also offers chemical composition analysis through Energy Dispersive X-ray Spectroscopy (EDS). This SEM analysis was performed using electrons focused under an acceleration voltage of about 20 keV. The Physical Property Measurement System (PPMS) Quantum Design DynaCool-9 served as a pivotal tool in conducting an exhaustive exploration into the distinctive magnetic properties inherent to the samples under scrutiny. These analyses were executed using the PPMS in conjunction with a closed-cycle helium cryostat, ensuring an environment of controlled thermal stability. This advanced apparatus operates within a controlled temperature range spanning from 1.8 K to 400 K, thus facilitating meticulous analyses across a substantial thermal spectrum. Furthermore, this configuration affords the precise application of magnetic fields, spanning from 0 T to 6 T, thereby creating an ideal environment for a comprehensive investigation into the magnetic behaviors of materials under investigation.

3. Results and Discussions

3.1. XRD Analysis

X-ray diffraction (XRD) analysis was employed to determine the crystal structure of the synthesized material. Rietveld refinement, a comprehensive technique for analyzing XRD data, was utilized. As shown in Figure 1, the FullProf program was used for Rietveld analysis, and the obtained XRD data were compared with simulated diffraction patterns based on established crystallographic information [22]. This analysis provided valuable insights into the crystallographic properties, lattice parameters, and symmetry of the samples. In the Rietveld analyses conducted in previous studies, a very common occurrence observed during x = 0.5 doping of the Ba element is the formation of the BMO phase along with the LBMO main phase. The addition of Ba to the structure alters the electrical charge balance, resulting in changes in the Mn−O−Mn bond angle and length due to radius

24

incompatibility, leading to the emergence of BMO impurities in the perovskite structure. The XRD results presented in Table 1 revealed that the main phase, the LBMO perovskite compound, exhibited a cubic crystal structure (*Pm3m* space group) [9], [17], [21]. Conversely, the $BaMnO_3$ nanorods, identified as the second phase, adopted a hexagonal crystal structure and space group *P63/mmc* [4], [18], [23]. The small peak marked with * in the XRD pattern between 28.65° and 29.43° was attributed to La_2O_3 [24]−[27]. In the XRD analysis, trace amounts of La elements, which could not incorporate into the main structure, were detected as impurities in the form of the La_2O_3 compound.
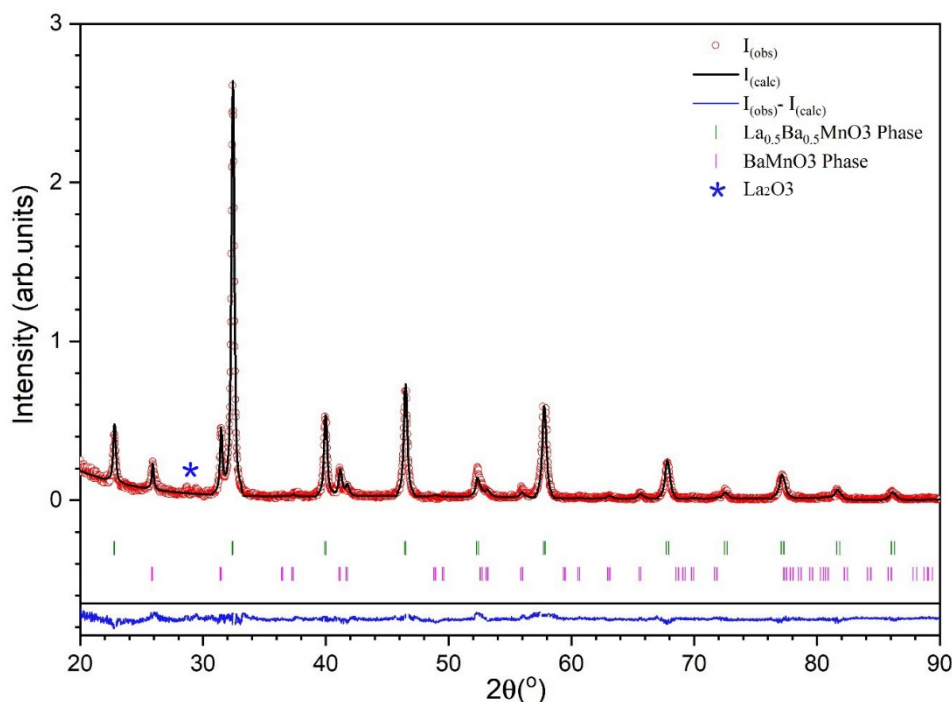

Figure 1. Observed and calculated XRD data and Rietveld refinement for $La_{0.5}Ba_{0.5}MnO_3−BaMnO_3$

Table 1. X-ray analysis of sample $La_{0.5}Ba_{0.5}MnO_3−BaMnO_3$ unit cell parameters for Rietveld refinements

	$La_{0.5}Ba_{0.5}MnO_3$	$BaMnO_3$
Crystal Structure	Cubic	Hexagonal
Space Group	Pm3m	P63/mmc
a(Å)	3.9108	5.6954
b(Å)	3.9108	5.6954
c(Å)	3.9108	4.8224
V(Å)³	59.8115	135.4692
Mn-O-Mn (º)	180	-
Mn-O1 (Å)	1.95538	-
GoF	1.3	1.3
Phase Fract (%)	**80.25**	**19.75**
Rp	13.9	13.9
Rwp	17.9	17.9
Re	12.1	12.1
X^2	2.4	2.4

3.1.2. SEM-EDS Analysis

Figure 2 presents SEM images of the LBMO sample surface at various magnifications. In the

25

SEM image (Figure 2a) taken at 15 kX magnification, two different structures stand out. The main phase exhibits a granular structure, while the second phase was formed in the form of rod-like structures. These randomly distributed rod-like structures were investigated in detail by SEM. On the other hand, in figure 2 g and h, in order to better understand and investigate rod-like structures, a single nanorod was isolated onto the adhesive carbon conductive tape surface for structural analysis using SEM techniques. The graph in Figure 2 a shows the result obtained in the ImageJ program used to calculate the particle distribution analysis revealed that the average particle size for the main phase was 59.83 nm (~60 nm). To gain a better understanding of the nanorods formed on the surface and to determine their formation within the main structure, SEM images were captured at various magnifications from different regions of the sample surface (Figure 2-b,c,d,e,f). In the SEM image taken at 30 kX magnification in Figure 2e, it is observed that the main structure is distributed homogeneously and the particle size is almost equal everywhere, while the other phase (BMO) grows randomly and moving away the structure. It is also observed that these structures are not uniform and their thickness and length vary from place to place. Figure 2f depicts an SEM image with magnification values of up to 140 kX, revealing a homogeneous distribution of particles in the main structure. Additionally, another phase (BMO) with regular cross-sections and a smooth surface is observed. These SEM images (Figure 2: a-f , respectively) revealed a distinct structure formed outside the main LBMO. The smooth morphology of the rod-like structures and the underlying granular LBMO matrix suggest a random distribution throughout the sample surface. The SEM images in Figure 2g and h illustrate the presence of a nanorod structure with smooth cross-sections, distinct from the main structure. In Figure 2h, the underlying surface is the adhesive carbon conductive tape.

In Figure 3, an attempt was made to select the largest area by going to the 5 kX value of the sample at low magnification. For EDS analysis, area and point scans were made for approximately 12 different regions. The EDS detector collected characteristic X-rays and provides elemental composition (by weight percentage) data in the table in Figure 3. The random distribution of the rods on the surface in the region taken for SEM–EDS analysis is noteworthy. Overall, the average composition value of the compound $La_{0.5}Ba_{0.5}MnO_3$ confirms that the desired stoichiometry has been achieved. In particular, the purple colored areas in the table (spectrums 7 and 10) correspond to regions on rod-like structures and exhibit lower La content and higher Ba content compared to the average composition. The XRD analysis suggests that the absence of trace amounts of La element in these two regions is attributed to the formation of the La_2O_3 phase and its subsequent removal from the structure. Consequently, the x-ray reflections collected from the nanorods on the surface are more pronounced, leading to the detection of an excess of Ba content with EDS detector.
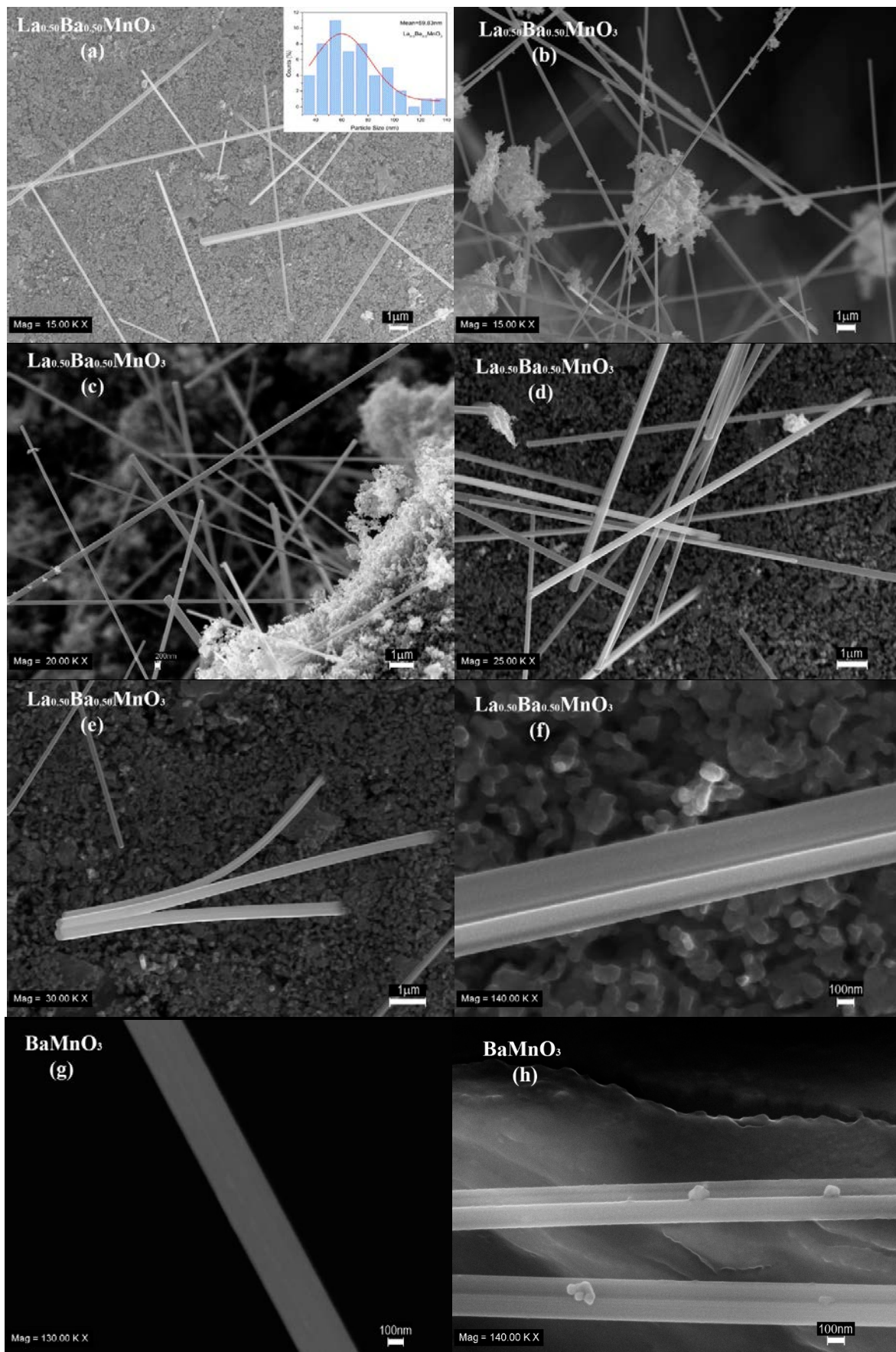
Figure 2. Magnifications of SEM images, a,b) 15kX c) 20kX d) 25kX e) 30kX c) 140kX La$_{0.5}$Ba$_{0.5}$MnO$_3$ and g) 130kX, h) 140kX is BaMnO$_3$ nanorod.

To accurately determine the composition of these nano-sized structures, EDS analysis was conducted on a single nanorod extracted from the surface (Figure 2g). As shown in Figure 3, EDS analysis of the isolated nanorod was taken from four different regions, confirming that this nanostructure is $BaMnO_3$ as a result of the EDS. This finding supports the two-phase structure observed in the XRD analysis and correlates the presence of rod-like structures observed in the SEM images with the $BaMnO_3$ phase. Therefore, $BaMnO_3$ nanorods can be defined as impurities formed independently on the surface of the LBMO perovskite manganite. Particle size analysis revealed that these nanorods had a thickness range of 100 to 250 nm and a length of 5 to 20 μm. This comprehensive analysis of SEM and EDS results revealed the homogeneity of the sample, both in terms of phase distribution and adherence to the desired stoichiometric ratio.
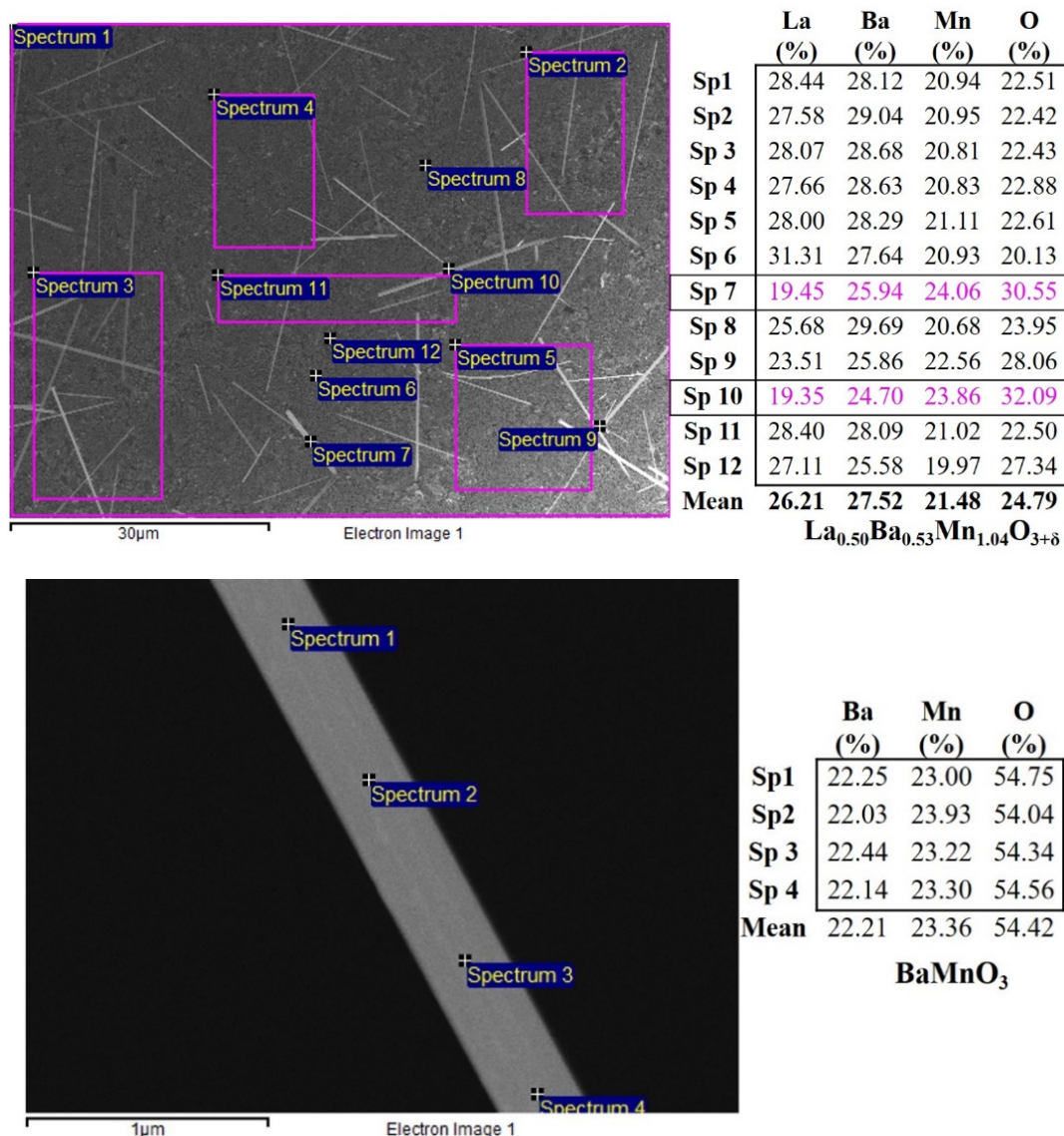
	La (%)	Ba (%)	Mn (%)	O (%)
Sp1	28.44	28.12	20.94	22.51
Sp2	27.58	29.04	20.95	22.42
Sp 3	28.07	28.68	20.81	22.43
Sp 4	27.66	28.63	20.83	22.88
Sp 5	28.00	28.29	21.11	22.61
Sp 6	31.31	27.64	20.93	20.13
Sp 7	19.45	25.94	24.06	30.55
Sp 8	25.68	29.69	20.68	23.95
Sp 9	23.51	25.86	22.56	28.06
Sp 10	19.35	24.70	23.86	32.09
Sp 11	28.40	28.09	21.02	22.50
Sp 12	27.11	25.58	19.97	27.34
Mean	26.21	27.52	21.48	24.79

$La_{0.50}Ba_{0.53}Mn_{1.04}O_{3+\delta}$

	Ba (%)	Mn (%)	O (%)
Sp1	22.25	23.00	54.75
Sp2	22.03	23.93	54.04
Sp 3	22.44	23.22	54.34
Sp 4	22.14	23.30	54.56
Mean	22.21	23.36	54.42

$BaMnO_3$

Figure 3. EDS analysis % Weight for $La_{0.5}Ba_{0.5}MnO_3$ perovskite naoparticles and $BaMnO_3$ nanorod.

3.1.3. Magnetic Properties

The investigation encompassed magnetization measurements as functions of both temperature and magnetic field, denoted as M(T) and M(H) respectively. These analyses were executed using the Quantum Design Physical Properties Measurement System (PPMS) in conjunction with a closed-

cycle helium cryostat, ensuring an environment of controlled thermal stability. Figure 4a showcases M(T) measurements conducted under various conditions, including zero field cooling (ZFC) and field cooling (FC) at a magnetic field strength of 50 Oe (5 mT). This extensive procedure covered a temperature range from 5 K to 400 K. Based on both XRD and SEM−EDS data, it is evident that two distinct phases are formed in the structure upon Ba doping. This observation has also influenced magnetic measurements. Spin-glass interactions may arise due to the presence of antiferromagnetic regions (BMO) within a compound (LBMO) predominantly exhibiting ferromagnetic properties. Furthermore, the significant gap between the ZFC and FC curves at lower temperatures supports this interaction. By analyzing the FC curve in Figure 4a, the T_C value was determined to be 323K, corresponding to the peak of the dM/dT curve [19], [20], [29].

To evaluate the effect of the paramagnetic phase using the Curie–Weiss law in equation (1), we examined the slope of the reverse susceptibility (1/χ) as a function of temperature using the FC curve (Fig. 4b). The red line in the graph represents the Curie-Weiss fit, while the θ_{CW} value represents the paramagnetic Curie-Weiss temperature value (where C in the equation is the Curie constant). If θ_{CW} is greater than T_C, it indicates the presence of magnetic inhomogeneity [12], [30]. Furthermore, M(H) measurements Figure 4c were executed meticulously for the sample. This process involved intervals of 4 K, encompassing temperatures both above and below the T_C value. The magnetic field strength extended up to 6 T, thereby encapsulating a substantial range of magnetic conditions. The intricate assessment of the magnetic entropy change ($-\Delta S_M$) values necessitated the utilization of data derived from the M(H) measurements (Figure 4c). Central to this analysis was Maxwell's thermodynamic equation (2) and if the system is in thermodynamic equilibrium, this formula turns into an integral (3), (4) this equation played a pivotal role in the precise calculation of the magnetic entropy change values. For simplicity, the integral expression (2) was approximated using a summation, wherein the derivative within the integral was discretized using finite differences [31], [32]. These calculations were based on discrete magnetization values acquired at distinct temperatures and applied magnetic fields, as outlined in the following expression (5) Here, ($-\Delta S_M$) represents the magnetic entropy change at temperature T_i. The values of M_i and M_{i+1} correspond to the experimental magnetization at temperatures T_i and T_{i+1}, respectively, under the influence of the magnetic field H_i, employing this comprehensive methodology, the precise quantification of $-\Delta S_M$ values was achieved (Figure 4d). $-\Delta S_M$ was observed to be 0.62 J/kgK at a magnetic field of 1 T and 2.25 J/kgK at a magnetic field of 6 T, as determined from the M(H) curves. The wide maximum value distribution of $-\Delta S_M$ around the T_C in LBMO is a desirable property for electronic applications. Future studies will investigate whether the T_C is increased or decreased by the formation of $BaMnO_3$ nanorods. This approach provided invaluable insights into the magnetic characteristics of the examined materials, thus enriching our understanding of their potential applications within novel magnetic cooling prototype.
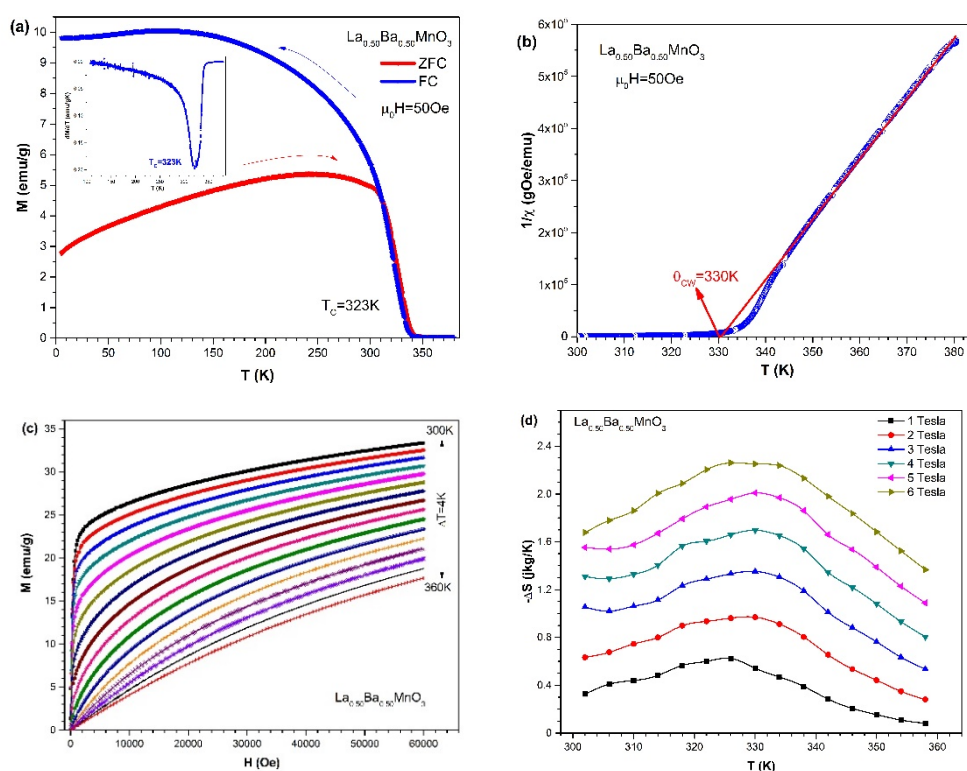
OPEN JOURNAL OF
NANO

Figure 4. a) M(T) curves of the compounds obtained using ZFC and FC, insets: dM/dT (T) curve b) $1/\chi$ (T) curve and c) M(H) curves of the compounds at 1T to 6 T for both below and above T_C, d) Temperature dependences of $-\Delta S_M$ at several magnetic field changes for $La_{0.5}Ba_{0.5}MnO_3$.

4. Conclusions

In this study, half-doped $La_{0.5}Ba_{0.5}MnO_3$ perovskite manganite compound was successfully obtained using the sol-gel method. It was confirmed by SEM−EDS analysis that the main compound showed a homogeneous particle distribution and the presence of BMO nanorods, regardless of the main structure. XRD refinement revealed that the crystal structure of the synthesized material comprised two distinct phases: the main phase consisting of 80.25% LBMO and a secondary phase comprising 19.75% BMO nanorods. Additionally, it was determined that the trace amount of La element not incorporated into the main structure existed in the form of La_2O_3. Detailed SEM analysis revealed that the secondary phase was present in the form of nanorods randomly distributed on the surface, with varying lengths and widths. Furthermore, EDS analysis confirmed the composition of these nanorods, with the composition identified XRD analysis as $BaMnO_3$. It is worth noting that each nanorod exhibits a uniform width along its entire length, a characteristic commonly observed in the hydrothermal production method, not seen in the sol-gel method [33]. Magnetization measurements revealed that the Curie transition temperature of the LBMO sample was determined to be 323 K. Literature reports have shown Curie transition temperature values for LBMO samples ranging from 270 K to 335 K [7]–[9], [33], [35]–[37]. The aim is to produce a material exhibiting a magnetic phase transition close to room temperature. Discrepancies in Curie temperatures among LBMO samples in the literature stem from variations in production methods, sintering temperature and sintering time. Moreover, it was observed that the formation of BMO nanorods on the surface of the LBMO sample obtained in this study resulted in the removal of a certain amount of Mn atoms. It is hypothesized that alterations in the bond angle and lengths (Mn−O−Mn) of Mn atoms departing from this structure, along with the reduction in Mn atoms, which serve as magnetic moment carriers,

30

contribute to raising the ferromagnetic to paramagnetic phase transition in LBMO above to room temperature [34]. The isothermal magnetic entropy change of the LBMO sample was calculated using magnetization measurements. The sample exhibited a magnetic entropy change (−ΔSM) of 0.62 J/kgK and 2.25 J/kgK at applied fields of 1 T and 6 T, respectively. Examination of the −ΔSM graph reveals a very wide distribution around TC. This broad distribution is a desirable characteristic for magnetic cooling applications in perovskite materials. While the LBMO sample demonstrates a TC close to room temperature, making it a candidate for magnetic cooling materials, its relatively low entropy change suggests limitations in achieving high relative cooling power (RCP). The formation of BMO nanorods in LBMO was identified as another key factor affecting its magnetic properties. These nanorods can provide new magnetic interactions for nanosensors, field effect transistor (FET), ferroelectricity, energy storage, biosensors, dielectric materials and are thought to provide useful information in future studies [18]–[23]. Overall, this work adds new insights into the interaction between Ba substitution and the formation of BMO nanorods on LBMO. Additionally, our findings suggest that LBMO is a promising candidate for various applications, including spintronic devices, magnetic sensors, and other electronic devices. Moreover, the substitution of La with Ba in LBMO resulting in the formation of $BaMnO_3$ nanorods as the second step is thought to be due to the effect of a relatively low sintering temperature and rapid cooling process on the composite. This is a new observation and may have important implications in the development of new materials with specific magnetic properties. Our findings indicate that LBMO is a promising candidate for a wide range of applications and that Ba substitution can be used to tailor the magnetic properties of LBMO to specific applications.

Equations:

$$\chi = \frac{C}{T - \theta_{CW}} \qquad (1)$$

$$\left(\frac{\partial S(H,T)}{\partial H}\right)_T = \left(\frac{\partial M(H,T)}{\partial T}\right)_H \qquad (2)$$

$$\Delta S_M(T)_{\Delta H} = \int_0^H dS_M(T,H)_T = \int_{H_0}^{H_1} \left(\frac{\partial M(T,H)}{\partial T}\right)_H dH \qquad (3)$$

$$-\Delta S_M(T,M) = \int_0^H \left(\frac{\partial M}{\partial T}\right)_H dH \qquad (4)$$

$$-\Delta S_M(H,T) = \sum_i \frac{M_i - M_{i+1}}{T_{i+1} - T_i} \Delta H_i \qquad (5)$$

References

[1] Keshri, S., Kumar, V., Wiśniewski P. & Kamzin, A.S. (2014). Synthesis and characterization of LSMO manganite-based biocomposite. Phase Transitions, 87 (5), 468-476.

[2] Coşkun, A.T., Çetin, S. K. & Ekicibil, A. (2022). The investigation of the effect of K doping on the structural, magnetic, and magnetocaloric properties of $La_{1.4-x}K_xCa_{1.6}Mn_2O_7$ $(0.0 \leq x \leq 0.4)$ double perovskite manganite. J Mater Sci: Mater Electron, 33, 10990–11001.

[3] Autreta, C., Martina, C., Hervieua, M., Maignana, A., Raveaua, B., Andreb, G., Bouree, F. & Jirakc, Z. (2003) From A-type antiferromagnetism to ferromagnetism in half-doped perovskite manganites. Journal of Magnetism and Magnetic Materials, 270, 194–202.

[4] Trukhanov, S.V., Trukhanov, A.V., Stepin, S.G., Szymczak, H. & Botez, C.E. (2008). Effect of the Size Factor on the Magnetic Proeperties of Manganite $La_{0.5}Ba_{0.5}MnO_3$. Physics of the Solid State-Magnetism and Ferroelectricity, 50, 5, 886-893.

[5] Gan, J., Hou, N., Yao, T., Fan, L., Gan, T., Huang, Z., Zhao, Y. & Li, Y. (2020). A high performing perovskite cathode with in situ exsolved Co nanoparticles for H_2O and CO_2 solid oxide electrolysis cell. Catalysis Today, 364, 89–96.

[6] Liang, S., Xu, T., Teng, F., Zong, R. & Zhu, Y. (2010). The high activity and stability of $La_{0.5}Ba_{0.5}MnO_3$ nanocubes in the oxidation of CO and CH_4. Applied Catalysis B: Environmental, 96, 267–275.

[7] Spooren, J., Walton, R.I. & Millange, F. (2005). A study of the manganites $La_{0.5}M_{0.5}MnO_3$ (M= Ca, Sr, Ba) prepared by hydrothermal synthesis. J. Mater. Chem., 15, 1542–1551.

[8] Millange, F., Caignaert, V., Domenge`s, B. & Raveau, B. (1983). Order-Disorder Phenomena in New $LaBaMn_2O_{6-x}$ CMR Perovskites. Crystal and Magnetic Structure. Chem. Mater. 10, 1977.

[9] Pękała, M., Drozd, V., Fagnard, J. F., Vanderbemden, P., & Ausloos, M. (2009). Magnetotransport of $La_{0.5}Ba_{0.5}MnO_3$. Journal of Applied Physics, 105(1).

[10] Trukhanov, S.V., Trukhanov, A.V., Botez, C.E. & Szymczak, H. (2009). Magnetic Properties of the $La_{0.5}Ba_{0.5}MnO_3$ Nanomanganites. Solid State Phenomena, 152/153, 135-138.

[11] Millange, F., Suard, E., Caignaert, V. & Raveau, B. (1999). $YBaMn_2O_5$: crystal and magnetic structure reinvestigation. Materials Research Bulletin, 34, 1, 1-9.

[12] Trukhanov, S. V., Trukhanov, A. V., Botez, C. E., & Szymczak, H. (2009). Magnetic properties of the $La_{0.50}Ba_{0.50}MnO_3$ nanomanganites. Solid State Phenomena, 152, 135-138.

[13] Zhou, R., Yin, Y., Dai, H., Yang, X., Gu, Y., & Bi, L. (2023). Attempted preparation of $La_{0.5}Ba_{0.5}MnO_{3-\delta}$ leading to an in-situ formation of manganate nanocomposites as a cathode for proton-conducting solid oxide fuel cells. Journal of Advanced Ceramics, 12(6)

[14] Xia, W., Leng, K., Tang, Q., Yang, L., Xie, Y., Wu, Z., & Zhu, X. (2021). Structural characterization and magnetic properties of single-crystalline $(La_{0.6}Pr_{0.4})_{0.67}Ca_{0.33}MnO_3$ nanowires. Journal of the American Ceramic Society, 104(10), 5402-5410.

[15] Modeshia, D. R., & Walton, R. I. (2010). Solvothermal synthesis of perovskites and pyrochlores: crystallisation of functional oxides under mild conditions. Chemical Society Reviews, 39(11), 4303-4325.

[16] Zhu, D., Zhu, H., & Zhang, Y. (2002). Hydrothermal synthesis of $La_{0.5}Ba_{0.5}MnO_3$ nanowires. Applied physics letters, 80(9), 1634-1636.

[17] Chai, P., Liu, X., Wang, Z., Lu, M., Cao, X. & Meng, J. (2007). Tunable synthesis, growth mechanism, and magnetic properties of $La_{0.5}Ba_{0.5}MnO_3$. Crystal Growth and Design, 7(12), 2568-2575.

[18] Hu C.G., Liu H., Lao C.S., Zhang L.Y., Davidovic D. & Wang Z.L. (2006). Size-manipulable synthesis of single-crystalline $BaMnO_3$ and $BaTi_{1/2}Mn_{1/2}O_3$ nanorods/nanowires. J Phys Chem B., 110(29):14050-4.

[19] Rondinelli, J. M., Eidelson, A. S. & Spaldin, N. A. (2009). Non-d 0 Mn-driven ferroelectricity in antiferromagnetic BaMnO 3. Physical Review B, 79(20), 205119.

[20] Kandemir, A., Akça, G., Kılıç Çetin, S., Ayaş, A. O., Akyol, M. & Ekicibil, A. (2023) Effects of Ca substitution on magnetic and magnetocaloric properties in $PrBa_{1-x}Ca_xMn_2O_6$ system. Journal of Solid State Chemistry, 324, 124086.

[21] Thakur, P., Kumari, S., Chaudhary, S., Sharma, N., & Lal, M. (2024). Multifunctional tuning of structural, dielectric, and magnetic properties of Ti-doped $BaMnO_3$ ceramics. Emergent Materials, 1-20.

[22] Roisnel, T. & Rodriguez-Carvajal, J. (2003) Computer Program FULLPROF, LLB-LCSIM.

[23] Terenti, N., Melnic, E., Fruth, V., Nedelko, N., Aleshkevych, P., Lewińska, S., Ślawska-Waniewska, A., Kravtsov, V. Ch., Lazarescu, A. & Lozan, V. (2023). Synthesis and microstructure of BaMnO3 oxide obtained from coordination precursor, Journal of Solid State Chemistry, 324

[24] Razmara, Z. (2019) Lanthanum (III) complex as ferromagnetic supraprecursor for preparation of La_2O_3 nanoparticles by thermal decomposition method. Research on Chemical Intermediates, 45, 2887-2901.

[25] Pathan, A. A., Desai, K. R., Vajapara, S. & Bhasin, C. P. (2018) Conditional Optimization of Solution Combustion Synthesis for Pioneered La_2O_3 Nanostructures to Application as Future CMOS and NVMS Generations. Advances in Nanoparticles 7, 1, 28-35.

[26] Mustofa, K., Yulizar, Y., Saefumillah, A. & Apriandanu, D.O.B. (2020). La_2O_3 nanoparticles formation using Nothopanax scutellarium leaf extract in two-phase system and photocatalytic activity under UV light irradiation. IOP Conference Series: Materials Science and Engineering, 902, 1, 012018.

[27] Hu, C. G., Liu, H., Dong, W. T., Zhang,Y. Y., Bao, G., Lao, C. S. & Wang, Z. L. (2007). $La(OH)_3$ and La_2O_3 Nanobelts- Synthesis and Physical Properties. Advanced Materials, 19, 3, 470-474.

[28] Hu, C., Liu, H. & Wang, Z. L. (2008). Synthesis of Oxide Nanostructures. BioNanofluidic MEMS, 11-36.

[29] Chau, N., Hanh, D. T., Tho, N. D. & Luong, N. H. (2006). Spin glass-like behavior, giant magnetocaloric and giant magnetoresistance effect in PrPb manganites. Journal of Magnetism and Magnetic Materials, 303(2), e335-e338.

[30] Munazat, D. R., Kurniawan, B., Razaq, D. S., Manawan, M., Shon, W. H., Rhyee, J. S. & Nanto, D. (2024). Effect of Zn substitution on magnetic properties and magnetic entropy change in $La_{0.7}Ba_{0.25}Nd_{0.05}Mn_{1-x}Zn_xO_3$ (x= 0.03 and 0.05) synthesized by using sol-gel method. Physica B: Condensed Matter, 415800.

[31] Al-Shahumi, T. M., Al-Omari, I. A., Al-Harthi, S.H. & Myint, M. T. Z. (2023) Synthesis, structure, morphology, magnetism, and magnetocaloric-effect studies of $(La_{1-x}Pr_x)_{0.7}Sr_{0.3}MnO_3$ nanocrystalline perovskites. SN Applied Sciences, 5, 121.

33

[32] Iqbal, M., Nasir Khan, M., A.Khan, A., Zaka, I., Mehmood, A. & Ahmad, I. (2018). Investigation of Magnetic, Magnetocaloric, and Critical Properties of $La_{0.5}Ba_{0.5}MnO_3$ Manganite. Journal of Superconductivity and Novel Magnetism, 31, 3535–3544.

[33] Zhu, D., Zhu, H., & Zhang, Y. (2003). Microstructure and magnetization of single-crystal perovskite manganites nanowires prepared by hydrothermal method. Journal of Crystal Growth, 249(1-2), 172-175.

[34] Dinçer, İ. (2005). $PrMn_{1.6}Fe_{0.4}Ge_2$ Alaşımının Curie Sıcaklığı Üzerindeki Antiferromanyetik Yapısı. Selçuk Üniversitesi Fen Fakültesi Fen Dergisi, 1(26), 33-42.

[35] Nakajima, T., Yoshizawa, H., & Ueda, Y. (2004). A-site randomness effect on structural and physical properties of Ba-based perovskite manganites. Journal of the Physical Society of Japan, 73(8), 2283-2291.

[36] Kawasaki, Y., Minami, T., Fujishima, M., Kishimoto, Y., Ohno, T., Zenmyo, K., & Ueda, Y. (2006). Ground state properties of the A-site ordered/disordered manganites $LaBaMn_2O_6/La_{0.5}Ba_{0.5}MnO_3$ probed by NMR. Physica B: Condensed Matter, 378, 525-526.

[37] Nagao, M., So, Y. G., Yoshida, H., Isobe, M., Hara, T., Ishizuka, K., & Kimoto, K. (2013). Direct observation and dynamics of spontaneous skyrmion-like magnetic domains in a ferromagnet. Nature nanotechnology, 8(5), 325-328.